Chemical Science

ROYAL SOCIETY OF CHEMISTRY

EDGE ARTICLE

View Article Online
View Journal | View Issue

Cite this: *Chem. Sci.*, 2024, **15**, 2473

All publication charges for this article have been paid for by the Royal Society of Chemistry

Facile fabrication of Ni, Fe-doped δ-MnO_2 derived from Prussian blue analogues as an efficient catalyst for stable Li–CO_2 batteries†

Xiaoyang Chen,‡[a] Jian Chen, ‡[a] Yun Qiao, *[a] Yun Gao,[b] Siwei Fan,[a] Yijie Liu,[a] Li Li,[a] Yang Liu*[a] and Shulei Chou *[b]

Received 31st October 2023
Accepted 2nd January 2024

DOI: 10.1039/d3sc05794a

rsc.li/chemical-science

Rechargeable Li–CO_2 batteries are regarded as an ideal new-generation energy storage system, owing to their high energy density and extraordinary CO_2 capture capability. Developing a suitable cathode to improve the electrochemical performance of Li–CO_2 batteries has always been a research hotspot. Herein, Ni–Fe-δ-MnO_2 nano-flower composites are designed and synthesized by *in situ* etching a Ni–Fe PBA precursor as the cathode for Li–CO_2 batteries. Ni–Fe-δ-MnO_2 nanoflowers composed of ultra-thin nanosheets possess considerable surface spaces, which can not only provide abundant catalytic active sites, but also facilitate the nucleation of discharge products and promote the CO_2 reduction reaction. On the one hand, the introduction of Ni and Fe elements can improve the electrical conductivity of δ-MnO_2. On the other hand, the synergistic catalytic effect between Ni, Fe elements and δ-MnO_2 will greatly enhance the cycling performance and reduce the overpotential of Li–CO_2 batteries. Consequently, the Li–CO_2 battery based on the Ni–Fe-δ-MnO_2 cathode shows a high discharge capacity of 8287 mA h g^{-1} and can stabilize over 100 cycles at a current density of 100 mA g^{-1}. The work offers a promising guideline to design efficient manganese-based catalysts for Li–CO_2 batteries.

Introduction

Nowadays, the over-dependence on traditional fossil fuels and the continuous release of greenhouse gases (CO_2) have led to serious environmental problems and hindered the sustainable development of the world.[1,2] To reduce carbon emissions or repurpose CO_2, various chemical processes have been adopted to convert CO_2 into value-added carbon compounds, such as methanol, organic materials and plastics.[3–7] However, the conventional CO_2 reduction system usually shows less energy conversion efficiency than the ideal value, due to the complex multi-electron reaction on the surface of the electrode.[8–10] Therefore, direct electrochemical reduction of CO_2 through a new energy storage device is an ideal strategy. Currently, metal–CO_2 batteries, especially Li–CO_2 batteries, show great potential in novel electrochemical CO_2 reduction energy storage systems, due to their high energy density and reversible CO_2 drive.[11,12] Unfortunately, the development and exploration of Li–CO_2 batteries are still in the early stage, and their practical application is restricted by large polarization, poor cycle stability and low coulombic efficiency.[13–15]

Typically, the widely recognized electrochemical reaction of Li–CO_2 batteries is confirmed to be $4Li + 3CO_2 = 2Li_2CO_3 + C$ (E = 2.80 V *vs.* Li/Li^+).[16,17] However, it is found that Li_2CO_3, the discharge product of Li–CO_2 batteries, is a kind of insulator with a wide band gap, and its decomposition kinetics is slow. As a result, Li_2CO_3, which is difficult to decompose, gradually accumulates on the surface of the cathode during cycling, inducing the coverage on the active sites of the catalyst and thus causing the cell deactivation.[18,19] Therefore, the study of cathodes with high catalytic activity to achieve reversible decomposition of Li_2CO_3 is a key strategy to improve the performance of Li–CO_2 batteries. Noble metal catalysts have been shown to promote the reversible formation and decomposition of Li_2CO_3 at lower potentials, greatly improving the electrochemical performance of Li–CO_2 batteries.[20–24] Nevertheless, their large-scale application is limited due to the high price and scarce reserves of noble metal catalysts.

Transition metal catalysts are considered as good substitutes for noble metal catalysts because of their excellent catalytic activity and relatively low cost.[25–27] Numerous studies have proved that MnO_2 catalyst can effectively promote the CO_2 reduction reaction (CO_2RR) and CO_2 evolution reaction (CO_2ER) processes.[28] In previous studies, Lei *et al.* reported that the α-MnO_2/CNT electrode could provide sufficient active sites for Li_2CO_3 nucleation and CO_2 capture, and the cathode structure

[a]*School of Environmental and Chemical Engineering, Shanghai University, Shanghai 200444, China. E-mail: yunqiao@shu.edu.cn; liuy986@163.com*

[b]*Institute for Carbon Neutralization, College of Chemistry and Materials, Engineering, Wenzhou University, Zhejiang 325035, China. E-mail: chou@wzu.edu.cn*

† Electronic supplementary information (ESI) available. See DOI: https://doi.org/10.1039/d3sc05794a

‡ X.-Y. C and. J. C. contributed equally to this work.

could be tuned.[29] Similarly, Wang *et al.* successfully synthesized the CNT@MnO_2 (Birnessite δ-MnO_2) cathode; the as-assembled Li–CO_2 batteries exhibited low overpotential and excellent cycle stability with the synergistic effect of δ-MnO_2 and CNTs.[30] However, further improvement of MnO_2 catalytic activity is restricted by its poor conductivity and limited active sites. Previous results have shown that the electrical conductivity of MnO_2 can be improved by modifying its band level and electronic structure through the introduction of atomic doping. Based on these inspirations, Peng *et al.* first applied Co-doped α-MnO_2 nanowires for Li–CO_2 batteries, achieving a low overpotential of 0.73 V and long cycle performance (500 cycles at 100 mA g^{-1}). They attributed the excellent electrochemical performance to the high conductivity of Co-α-MnO_2 nanowires, enhanced specific surface area, and synergistic catalysis of doped Co atoms.[31] However, its irregular pore size and low active specific surface area lead to non-uniform deposition of Li_2CO_3 and low discharge capacity, which will limit its practical application.

Herein, Ni, Fe co-doped δ-MnO_2 (Ni–Fe-δ-MnO_2) nanoflowers as a cathode for Li–CO_2 batteries were synthesized by *in situ* etching the Ni–Fe PBA precursors *via* a sacrificing-template strategy. Ni–Fe-δ-MnO_2 nanoflowers can significantly promote the CO_2RR and CO_2ER processes and improve the cycle stability of Li–CO_2 batteries. These excellent electrochemical properties are attributed to the unique nanoflower structure, abundant exposed surfaces, and a large number of oxygen vacancy defects of Ni–Fe-δ-MnO_2. Furthermore, the introduction of Ni and Fe elements can not only improve the conductivity of δ-MnO_2, but also significantly promote the reversible formation and decomposition of Li_2CO_3. Therefore, this work will provide an ideal guidance for the design of efficient Li–CO_2 battery cathodes in the future.

Results and discussion

Highly crystalline three-dimensional nanocubes with a uniform diameter of 50 nm were synthesized by the co-precipitation method, and are denoted as Ni–Fe-PBA (Fig. S1a and b†). As shown in Fig. 1, nanoflowers with a diameter of 170 nm are grown vertically and uniformly on the Ni–Fe-PBA template after the hydrothermal process, denoted as the Ni–Fe-δ-MnO_2 precursor (Fig. S1c and d†). Subsequently, Ni–Fe-δ-MnO_2 was obtained by calcining the Ni–Fe-δ-MnO_2 precursor in an Ar atmosphere at 300 °C for 2 h. The X-ray diffraction (XRD) characteristic peaks of Ni–Fe-δ-MnO_2 at 12.5°, 25.2°, 37.3°, and 65.6° can be well attributed to the (001), (002), (1 $\bar{1}$ 1), and (020) crystal faces of δ-MnO_2 (JCPDS no. 80-1098), as shown in Fig. 2a. Scanning electron microscopy (Fig. 2b and c) revealed that the morphology of Ni–Fe-δ-MnO_2 is well maintained compared with that of the Fe-δ-MnO_2 precursor, which means that these nanoflowers possess superior stability. Interestingly, the nanoflower structure exposes a large surface, which can provide a large space and rich active sites for the deposition and decomposition of discharge products. Meanwhile, no residues of other PBA-derived precursors are observed in the SEM images, which further indicates that Ni–Fe PBA has been completely etched during the hydrothermal process. Transmission electron microscopy (TEM) was performed to further demonstrate the cubic nanoflower morphology of Ni–Fe-δ-MnO_2 (Fig. 2d). It is worth noting that the ultra-thin nanosheets tend to bend and fold, and their thickness can be determined by measuring the folded area. The high-resolution transmission electron microscopy (HRTEM) image displays a lattice spacing of 0.67 nm, corresponding to the (001) plane of Ni–Fe-δ-MnO_2 (Fig. 2e). Furthermore, the thickness of the nanosheet is about 2.7 nm, corresponding to Ni–Fe-δ-MnO_2 (001) crystal surfaces.[32] Additionally, considerable micropores can be seen in Fig. 2f, which can provide more nucleation regions and oxygen vacancies, conducive to electron transport and nucleation of Li_2CO_3. The high-angle annular dark field-scanning transmission microscope (HAADF-STEM) image of Ni–Fe-δ-MnO_2 in Fig. 2g and the corresponding energy dispersive spectrometer (EDS) elemental mapping in Fig. 2h–l clearly prove the presence of Ni, Fe, Mn, and O elements in the catalyst, which are evenly distributed in Ni–Fe-δ-MnO_2 nanoflowers. It is worth noting that the presence of K element was also detected in the EDS spectrum, which was also verified by inductively coupled plasma mass spectrometry (ICP-MS) (Table S1†). This indicates that Ni–Fe-δ-MnO_2 contains a certain amount of K^+. The presence of K^+ can not only improve the structural stability and charge balance of MnO_2, but also promote the octahedral effect of MnO_6 and the diffusion rate of Li^+, which will further enhance the catalytic activities of the CO_2RR and CO_2ER.[33] The contents of Ni and Fe in Ni–Fe-δ-MnO_2 are 7.57 and 4.22 wt%, respectively, which means that Ni and Fe with a mass ratio of 2 : 1 occupy the surroundings of the MnO_6 octahedron. Thus, more oxygen vacancies are formed and can enhance the CO_2RR.

X-Ray photoelectron spectroscopy (XPS) was used to detect the valence state and electronic structure of Ni–Fe-δ-MnO_2, Ni–Fe-δ-MnO_2 precursor and δ-MnO_2. The XPS full spectra show obvious characteristic peaks of Fe, Ni, Mn, O and K elements (Fig. 3a), which are consistent with the EDS analysis results. As shown in Fig. 3b, the high-resolution Mn 2p XPS spectra exhibit three peaks, which can be divided into Mn^{4+} from MnO_2 at 642.2 eV, and the Mn^{3+} peaks at 654.0 and 645.4 eV due to the oxygen defects induced by Mn^{4+} transformation. The high-resolution O 1s XPS spectra of Ni–Fe-δ-MnO_2 were deconvoluted into three spin-orbital peaks at 529.46, 530.03, and 531.32 eV, corresponding to the lattice oxygen (O_1), oxygen vacancy (O_2), and hydroxyl or adsorbed water molecules (O_3) of Mn–O bonds (Fig. 3c). Ni–Fe-δ-MnO_2 has the highest O_2 ratio (45.97%), which further proves abundant oxygen vacancy defects in its structure.[34,35] As shown in Fig. 3d, the main peak of Ni $2p_{3/2}$ and its satellites at 854.9 and 861.4 eV, and the main peak of Ni $2p_{1/2}$ and its satellites at 872.2 and 879.3 eV are attributed to nickel in its oxides.[36] Similarly, the Fe 2p spectra (Fig. 3e) can be deconvoluted into five peaks at 710.4/723.5 eV (Fe^{3+}), 712.8/725.8 eV (Fe^{2+}) and 769.2 eV (satellite peaks).[37] The result can further confirm the successful synthesis of Ni–Fe-δ-MnO_2. As shown in Fig. 3d and e, both Ni 2p and Fe 2p peaks of Ni–Fe-δ-MnO_2 move to the lower binding energy in contrast to that of the Ni–Fe-δ-MnO_2 precursor, which can increase the density of the surrounding electron cloud. This phenomenon

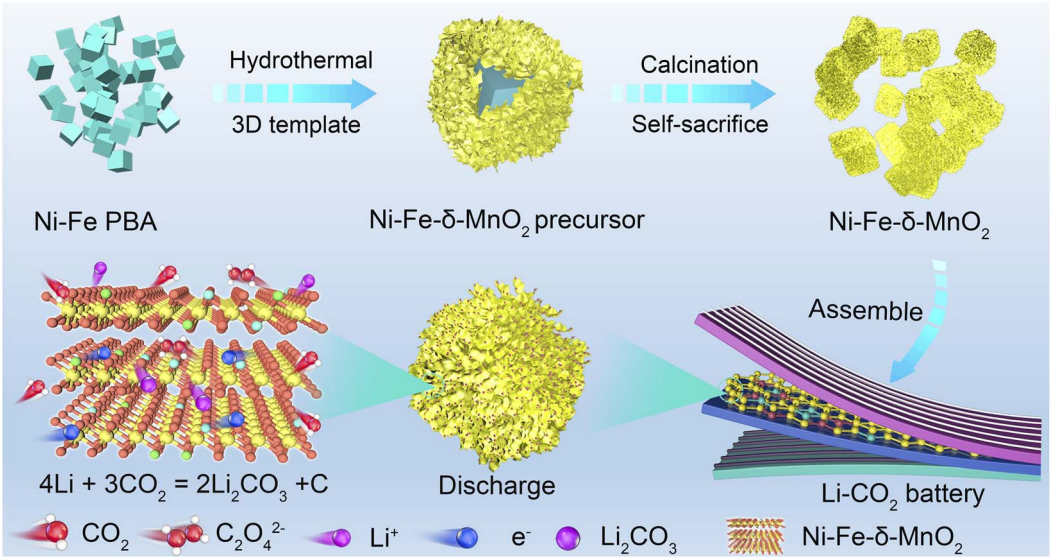

Fig. 1 Schematic illustration for the fabrication of the Ni–Fe-δ-MnO_2 cathode.

can be attributed to the co-coordination between Ni/Fe and O atoms in the center of Mn. In this case, this structure can inhibit Jahn–Teller distortion, stabilize the MnO_2 structure and expose more active sites. In addition, increasing the electron density of the metal center can enhance the adsorption between the metal center and the intermediate and change the coordination around MnO_2 to form more oxygen vacancies. Electron paramagnetic resonance (EPR) spectroscopy was employed to detect the unpaired electrons in Ni–Fe-δ-MnO_2. The EPR signal for Ni–Fe-δ-MnO_2 is dramatically enhanced in contrast to that of δ-MnO_2 and Ni–Fe-δ-MnO_2 precursor, which suggests its enhanced oxygen vacancy density (Fig. 3f).[38] Interestingly, the co-doping of Ni and Fe makes Ni–Fe-δ-MnO_2 expose more active sites and enhance the oxygen vacancy density through the coordination of adjacent O atoms around Mn, and thus promotes the activities of the CO_2RR and CO_2ER. Brunauer–

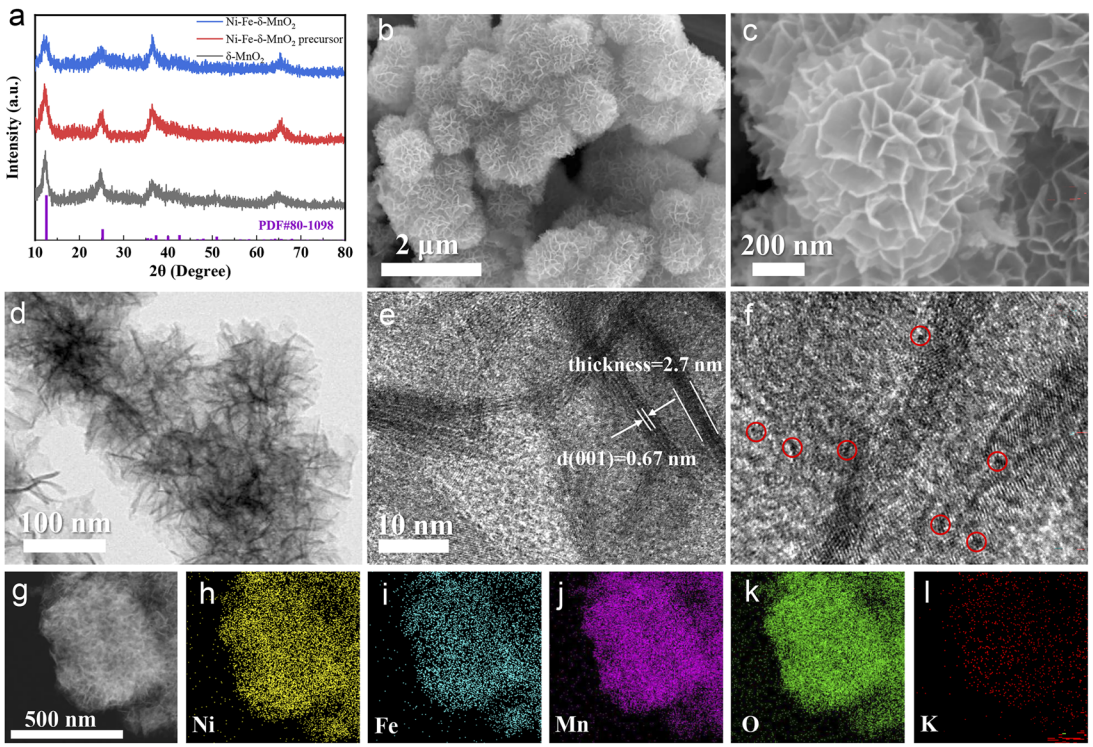

Fig. 2 (a) XRD patterns of δ-MnO_2, Ni–Fe-δ-MnO_2 precursor and Ni–Fe-δ-MnO_2, (b and c) SEM, (d) TEM, (e and f) HRTEM, (g) HAADF-STEM images and corresponding EDS elemental mapping results of (h) Ni, (i) Fe, (j) Mn, (k) O and (l) K elements for Ni–Fe-δ-MnO_2.

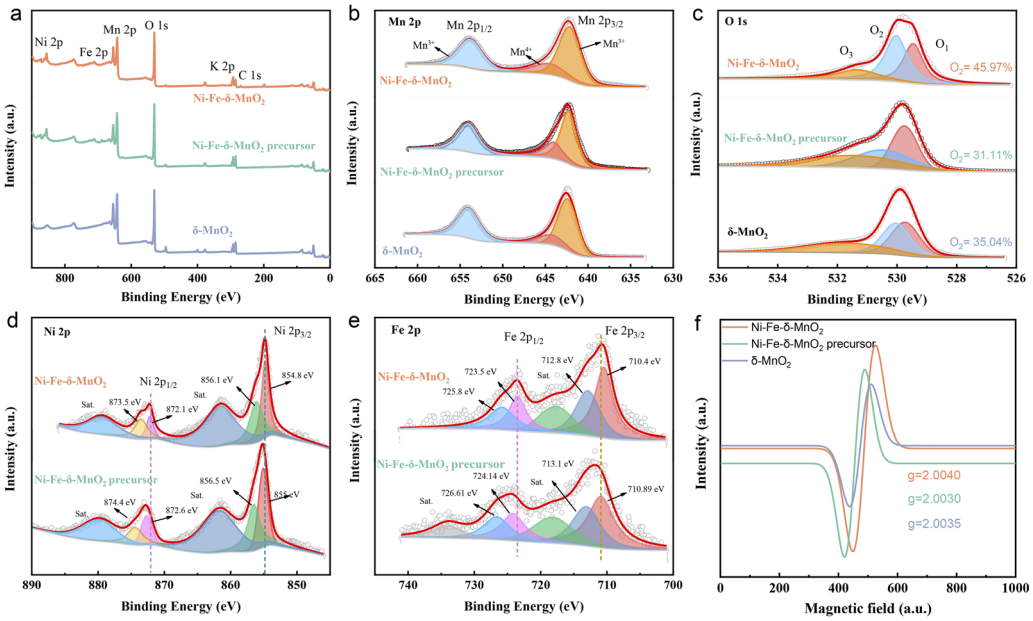

Fig. 3 (a) The survey XPS spectra, high-resolution XPS spectra of (b) Mn 2p, (c) O 1s of Ni–Fe-δ-MnO_2, Ni–Fe-δ-MnO_2 precursor and δ-MnO_2. High-resolution XPS spectra of (d) Ni 2p and (e) Fe 2p of Ni–Fe-δ-MnO_2 and Ni–Fe-δ-MnO_2 precursor. (f) EPR curves of Ni–Fe-δ-MnO_2, Ni–Fe-δ-MnO_2 precursor and δ-MnO_2.

Emmett–Teller (BET) analysis was applied to investigate the specific surface area of the as-prepared Ni–Fe-δ-MnO_2. The nitrogen adsorption and desorption curve (Fig. S2a†) shows that its specific surface area is up to 154.99 $m^2\ g^{-1}$ for Ni–Fe-δ-MnO_2, meaning that the catalyst can expose considerable active sites and provide sufficient space for the CO_2RR process. The pore size distribution results reveal that Ni–Fe-δ-MnO_2 possesses a large number of mesoporous structures with pore size in the range of 5.0–33.0 nm (Fig. S2b†). These mesoporous structures can accommodate more deposition of discharge products, enhance the diffusion of CO_2 and electrolyte, and expose more active sites. Based on the above analysis, we can conclude that Ni–Fe-δ-MnO_2 nanoflowers are successfully prepared. The presence of Ni and Fe elements can improve the electrical conductivity of δ-MnO_2. Moreover, their synergistic effect with Mn atoms will further improve the catalytic activity of the cathode. In addition, the large surface area and abundant oxygen vacancy defects for Ni–Fe-δ-MnO_2 can greatly enhance the reactivity of the CO_2RR and CO_2ER. Therefore, Ni–Fe-δ-MnO_2 nanoflowers are expected to be an ideal cathode for Li–CO_2 batteries.

The electrochemical performance of the Ni–Fe-δ-MnO_2 cathode in Li–CO_2 batteries was systematically evaluated. As shown in Fig. S3a,† the Ni–Fe-δ-MnO_2 cathode shows more obvious reduction and oxidation peaks in a CO_2 atmosphere than in an Ar atmosphere. In addition, Fig. S3b† reveals that the discharge capacity of the Ni–Fe-δ-MnO_2 cathode is 8287 mA h g^{-1}, which is 2.1 times that of the δ-MnO_2 cathode (3923 mA h g^{-1}), suggesting that the Ni–Fe-δ-MnO_2 cathode possesses a relatively better catalytic activity for the CO_2RR. In order to investigate the stability of the Li–CO_2 battery based on the Ni–Fe-δ-MnO_2 cathode, charge–discharge tests were conducted at a current density of 100 mA g^{-1} with a cutoff capacity of 1000 mA h g^{-1}. Fig. 4a and b display the charge and discharge cycles of Ni–Fe-δ-MnO_2 and δ-MnO_2 cathodes. The Li–CO_2 battery with Ni–Fe-δ-MnO_2 as the cathode can stabilize for 100 cycles, and its overpotential drops to 1.32 V (Fig. 4a). The charge terminal voltage remains below 4.2 V despite a slight increase after 100 cycles. As a contrast, we also investigated the cycle performance of δ-MnO_2 under the same test conditions, as shown in Fig. 4b. It is obvious that δ-MnO_2 exhibits extremely poor cycle stability. After 60 cycles, the voltage of its charging platform begins to gradually decrease. Unfortunately, both the terminal charge and discharge voltages reach the cut-off voltage (2.0 and 4.5 V) after 90 cycles. By comparing the discharge and charge terminal voltages of δ-MnO_2 and Ni–Fe-δ-MnO_2 (Fig. 4c), it can be clearly seen that the Ni–Fe-δ-MnO_2 exhibits much better cycle stability than δ-MnO_2. In addition, the overpotential of the Ni–Fe-δ-MnO_2 cathode is always lower than that of δ-MnO_2. Furthermore, we compared the overpotentials of the two cathodes at the 10th cycle (Fig. 4d). Compared with δ-MnO_2, the overpotential of the Ni–Fe-δ-MnO_2 is decreased by 0.23 V, further indicating that the introduction of Ni and Fe elements can significantly improve the catalytic activity of δ-MnO_2.

Fig. 4e exhibits the charge–discharge curves of the Li–CO_2 battery with Ni–Fe-δ-MnO_2 as the cathode at different current densities. When the current density increases from 400 to 1000 mA g^{-1}, the charge terminal voltage increases by only 0.13 V. The charge terminal voltage of Ni–Fe-δ-MnO_2 is only 4.43 V (<4.5 V) even at the current density of 1000 mA g^{-1}, indicating that the Ni–Fe-δ-MnO_2 electrode can still maintain excellent CO_2ER activity even at a higher current density. Furthermore, the electrochemical performance of the Ni–Fe-δ-MnO_2 cathode was compared with that of other Mn-based and related transition

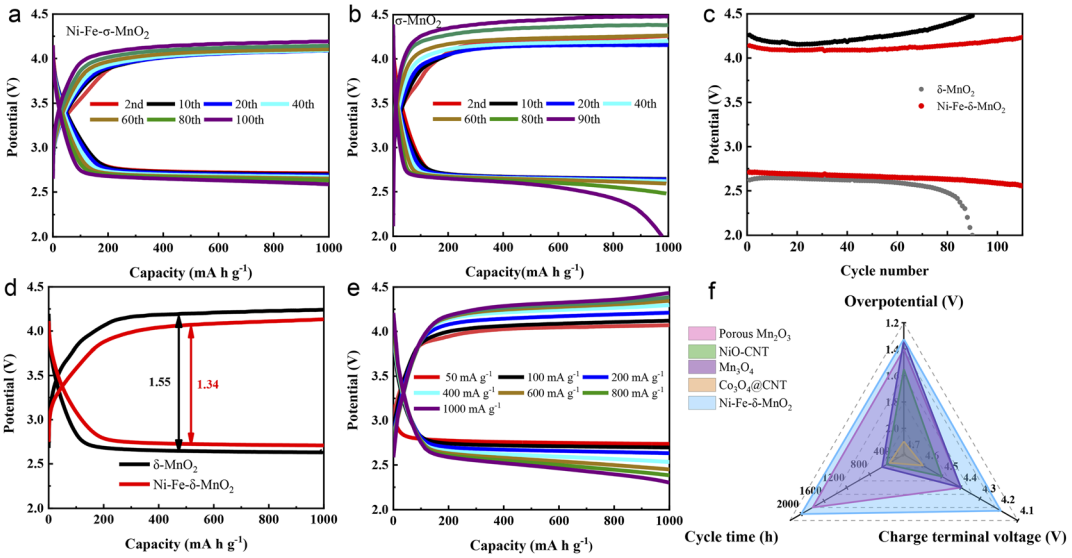

Fig. 4 The discharge and charge curves of (a) Ni–Fe-δ-MnO_2 and (b) δ-MnO_2 at 100 mA g^{-1} with a limited capacity of 1000 mA g^{-1}. (c) The discharge and charge terminal voltages of Ni–Fe-δ-MnO_2 and δ-MnO_2 upon cycling, (d) the overpotential comparison for the two cathodes at the 10th cycle. (e) The discharge and charge profiles of the Ni–Fe-δ-MnO_2 cathode at different current densities. (f) Comparison of the electrochemical properties of the Ni–Fe-δ-MnO_2 cathode and manganese based or other transition metal oxides.

metal catalysts. The radar diagram in Fig. 4f demonstrates that the Ni–Fe-δ-MnO_2 cathode endows obvious advantages in terms of cycle time, overpotential and charge terminal voltage.[39–42] These results indicate that Ni–Fe-δ-MnO_2 can improve the catalytic activities of the CO_2RR and CO_2ER, and thus significantly enhance the cycle stability of Li–CO_2 batteries.

In order to further explore the mechanism of the excellent electrochemical performance of the Ni–Fe-δ-MnO_2 cathode in a Li–CO_2 battery, SEM, XPS, *in situ* Raman and Fourier transform infrared (FTIR) spectroscopies were performed to systematically characterize the formation and decomposition of discharge products during the cycling processes. Fig. S6† displays the morphologies and structures of the Ni–Fe-δ-MnO_2 cathode at the discharged and recharged states. As shown in Fig. S6a,† discharge products with a flake morphology densely cover on the surface of the entire electrode after the first discharge process. Fortunately, the electrode returns to its pristine morphology, and the carbon nanotubes wrapped around its surface are also exposed after recharging (Fig. S6b†), indicating the reversible formation and decomposition of the discharge products. This result proves that the Ni–Fe-δ-MnO_2 electrode possesses excellent reversibility for the formation and decomposition of discharge products. In order to further verify the composition of the discharge products and the reversibility of the Ni–Fe-δ-MnO_2 electrode, the XPS spectrum was recorded. As shown in Fig. 5a, the high-resolution C 1s spectra can be deconvoluted into four distinct characteristic peaks at 284.96, 286.78, 290.45 and 293.53 eV after discharge, wherein the characteristic peak at 290.45 eV corresponds to the O–C=O bond of Li_2CO_3, indicating the existence of Li_2CO_3 as the discharge product. Importantly, this characteristic peak almost completely disappears after the subsequent recharging (Fig. 5b), demonstrating the reversibility of the discharge product. Fig. 5c shows the FTIR spectra of the pristine, discharged and recharged Ni–Fe-δ-MnO_2 cathodes. The discharged electrode exhibits three new peaks at 865, 1408 and 1476 cm^{-1}, compared with the pristine electrode, which are consistent with the standard spectrum of commercial Li_2CO_3.[43] Similarly, the characteristic peaks of Li_2CO_3 almost completely disappear in the subsequent recharging process, which is consistent with the XPS results. Moreover, we further investigated the electrochemical behaviour of the discharge product Li_2CO_3 in the whole charge and discharge processes by *in situ* Raman spectroscopy. As shown in Fig. 5d, the characteristic peaks of MnO_2 (633 cm^{-1}), D band (1343 cm^{-1}) and G band (1574 cm^{-1}) of carbon can be observed in the Raman spectra at the initial discharge stage. As the discharge progresses, the peak intensities of Li_2CO_3 (1081 cm^{-1}), D and G bands continuously increase, which can be attributed to the formation of discharge products (Li_2CO_3 and C).[44,45] In addition, the I_D/I_G ratio gradually decreases with the continuous discharge process, indicating that the C product possesses a high degree of graphitization. Noteworthily, higher graphitization is conducive to electron transfer and decomposition of discharge products, as the gradual weakening and eventual disappearance of Li_2CO_3 and C in the *in situ* Raman spectra during the subsequent charging process proves the complete decomposition of discharge products.[46] The corresponding 2D contour map in Fig. 5e further intuitively reflects this trend of evolution. These results fully demonstrate the reversible formation and decomposition of Li_2CO_3 during the cycling processes and the excellent catalytic activity of the Ni–Fe-δ-MnO_2 electrode for the CO_2RR and CO_2ER processes.[47] Besides, we can also notice that the characteristic peak of MnO_2 gradually disappears during the

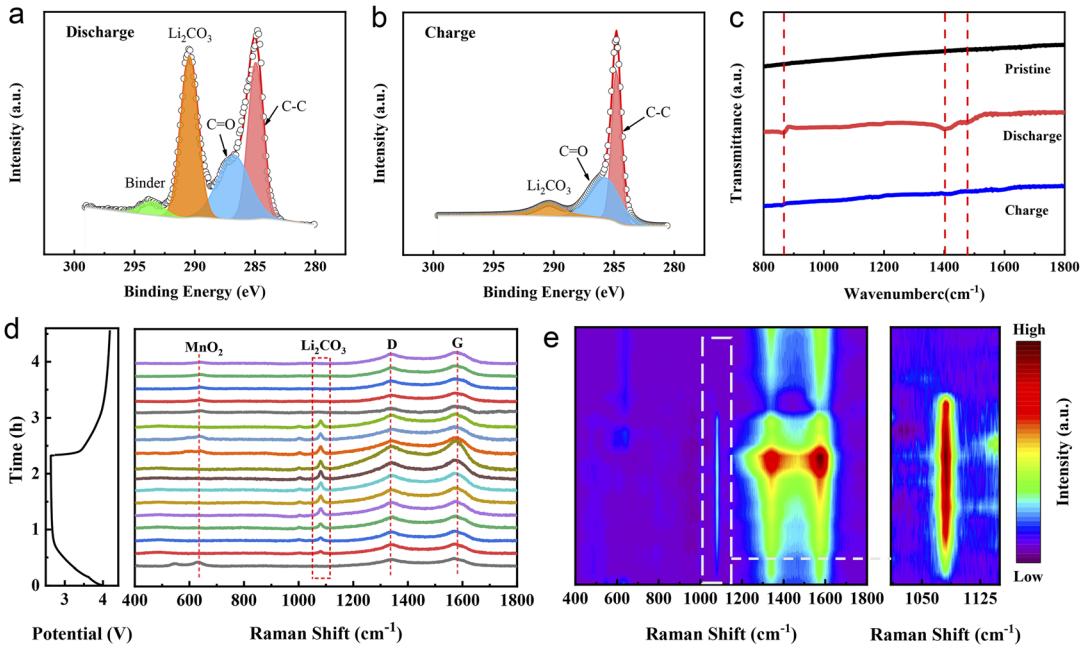

Fig. 5 The *ex situ* and *in situ* characterizations of the Ni–Fe-δ-MnO_2 cathode in Li–CO_2 batteries. XPS spectra of C 1s after (a) discharge and (b) charge processes. (c) FTIR spectra of the pristine, discharged and charged cathodes. (d) *In situ* Raman spectra and (e) the corresponding 2D contour plots of the Ni–Fe-δ-MnO_2 cathode.

discharge stage, which may be due to the coverage of Li_2CO_3 on the surface of the Ni–Fe-δ-MnO_2 electrode, which affects the detected signal of MnO_2. It is worth noting that the characteristic peak of MnO_2 appears with the gradual disappearance of Li_2CO_3, which is exactly opposite to the evolution trend of Li_2CO_3 after recharging. Furthermore, the existence of the MnO_2 signal after charging also indicates the stability of the Ni–Fe-δ-MnO_2 electrode. Based on the above results, we can conclude that Ni–Fe-δ-MnO_2 can promote not only the transport of electrons and Li^+ *via* the four-electron interaction but also the nucleation and reversible decomposition of Li_2CO_3, which could improve its catalytic performance.

Conclusions

In summary, Ni–Fe-doped δ-MnO_2 nanoflowers (Ni–Fe-δ-MnO_2) are designed and synthesized by etching a Ni–Fe-δ-MnO_2 precursor using the sacrificial template method. The Ni–Fe-δ-MnO_2 nanoflowers composed of ultra-thin nanosheets possess considerable surface spaces, which can not only provide abundant catalytic active sites, but also facilitate the nucleation of discharge products and promote the CO_2 reduction reaction. In addition, the introduction of Ni and Fe elements could improve the electrical conductivity of δ-MnO_2. It is worth noting that their synergistic catalytic effect with δ-MnO_2 could greatly enhance the cycling performance and reduce the overpotential of the Li–CO_2 battery. Due to these advantages, the Li–CO_2 battery with the Ni–Fe-δ-MnO_2 cathode delivers the highest discharge capacity of 8287 mA h g^{-1} at the current density of 100 mA g^{-1}, which is 2.1 times that of the bare δ-MnO_2. Additionally, the Li–CO_2 battery based on the Ni–Fe-δ-MnO_2 cathode can achieve a low overpotential of 1.32 V and outstanding cycle performance of 100 cycles. This work provides a reference direction for the design of highly efficient multi-atom co-catalysts in the future.

Data availability

Synthetic procedures, experimental details, and characterization data are available in the ESI.†

Author contributions

Y. Q., Y. L. and S. L. C. proposed the concept and supervised the work; X. Y. C. and J. C. designed the experiments and wrote the paper; S. W. F., Y. G., and Y. J. L. contributed to the discussion and provided suggestions. Y. J. L. helped to analyze the data; L. L. helped to summarize the data. All authors have discussed the results, drafted the manuscript and approved the final version of the manuscript.

Conflicts of interest

There are no conflicts to declare.

Acknowledgements

X.-Y. C. and J. C. contributed equally to this work. This work was financially supported by the National Natural Science Foundation of China (No. 51971124 and 52171217). The Innovative Research Team of High-level Local Universities in Shanghai is gratefully acknowledged for their financial support.

Notes and references

1 S. Ren, D. Joulié, D. Salvatore, K. Torbensen, M. Wang, M. Robert and C. P. Berlinguette, *Science*, 2019, **365**, 367.
2 Y. Zhou, F. Che, M. Liu, C. Zou, Z. Liang, P. de Luna, H. Yuan, J. Li, Z. Wang, H. Xie, H. Li, P. Chen, E. Bladt, R. Quintero-Bermudez, T.-K. Sham, S. Bals, J. Hofkens, D. Sinton, G. Chen and E. H. Sargent, *Nat. Chem.*, 2019, **11**, 1167.
3 K. S. Lackner, *Science*, 2003, **300**, 1677.
4 S. A. Theofanidis, A. N. Antzaras and A. A. Lemonidou, *Curr. Opin. Chem. Eng.*, 2023, **39**, 100902.
5 J. Zhang, R. Yin, Q. Shao, T. Zhu and X. Huang, *Angew. Chem., Int. Ed.*, 2019, **58**, 5609.
6 U. Ulmer, T. Dingle, P. N. Duchesne, R. H. Morris, A. Tavasoli, T. Wood and G. A. Ozin, *Nat. Commun.*, 2019, **10**, 3169.
7 I. Sullivan, A. Goryachev, I. A. Digdaya, X. Li, H. A. Atwater, D. A. Vermaas and C. Xiang, *Nat. Catal.*, 2021, **4**, 952.
8 R. Zhao, P. Ding, P. Wei, L. Zhang, Q. Liu, Y. Luo, T. Li, S. Lu, X. Shi, S. Gao, A. M. Asiri, Z. Wang and X. Sun, *Adv. Funct. Mater.*, 2021, **31**, 2009449.
9 D.-H. Guan, X.-X. Wang, M.-L. Li, F. Li, L.-J. Zheng, X.-L. Huang and J.-J. Xu, *Angew. Chem., Int. Ed.*, 2020, **59**, 19518.
10 X. Sun, X. Mu, W. Zheng, L. Wang, S. Yang, C. Sheng, H. Pan, W. Li, C.-H. Li, P. He and H. Zhou, *Nat. Commun.*, 2023, **14**, 536.
11 T. Jian, W. Ma, C. Xu, H. Liu and J. Wang, *eScience*, 2023, **3**, 100114.
12 Y.-F. Wang, G.-J. Ji, L.-N. Song, X.-X. Wang and J.-J. Xu, *ACS Energy Lett.*, 2023, **8**, 1026.
13 Y. Qiao, S. Xu, Y. Liu, J. Dai, H. Xie, Y. Yao, X. Mu, C. Chen, D. J. Kline, E. M. Hitz, B. Liu, J. Song, P. He, M. R. Zachariah and L. Hu, *Energy Environ. Sci.*, 2019, **12**, 1100.
14 J. Chen, X.-Y. Chen, Y. Liu, Y. Qiao, S.-Y. Guan, L. Li and S.-L. Chou, *Energy Environ. Sci.*, 2023, **7**, 130.
15 C. Yang, K. Guo, D. Yuan, J. Cheng and B. Wang, *J. Am. Chem. Soc.*, 2020, **142**, 6983.
16 X. Ma, W. Zhao, Q. Deng, X. Fu, L. Wu, W. Yan and Y. Yang, *J. Power Sources*, 2022, **535**, 231446.
17 D.-H. Guan, X.-X. Wang, F. Li, L.-J. Zheng, M.-L. Li, H.-F. Wang and J.-J. Xu, *ACS Nano*, 2022, **16**, 12364.
18 X.-X. Wang, D.-H. Guan, F. Li, M.-L. Li, L.-J. Zheng and J.-J. Xu, *Small*, 2021, **17**, 2100642.
19 B. Chen, D. Wang, J. Tan, Y. Liu, M. Jiao, B. Liu, N. Zhao, X. Zou, G. Zhou and H.-M. Cheng, *J. Am. Chem. Soc.*, 2022, **144**, 3106.
20 S. Yang, P. He and H. Zhou, *Energy Environ. Sci.*, 2016, **9**, 1650.
21 Z. Guo, J. Li, H. Qi, X. Sun, H. Li, A. G. Tamirat, J. Liu, Y. Wang and L. Wang, *Small*, 2019, **15**, e1803246.
22 C. Wang, Q. Zhang, X. Zhang, X.-G. Wang, Z. Xie and Z. Zhou, *Small*, 2018, **14**, e1800641.
23 S. Yang, Y. Qiao, P. He, Y. Liu, Z. Cheng, J.-j. Zhu and H. Zhou, *Energy Environ. Sci.*, 2017, **10**, 972.
24 H. Zhao, D. Li, H. Li, A. G. Tamirat, X. Song, Z. Zhang, Y. Wang, Z. Guo, L. Wang and S. Feng, *Electrochim. Acta*, 2019, **299**, 592.
25 S. Thoka, C.-J. Chen, A. Jena, F.-M. Wang, X.-C. Wang, H. Chang, S.-F. Hu and R.-S. Liu, *ACS Appl. Mater. Interfaces*, 2020, **12**, 17353.
26 A. Hu, C. Shu, C. Xu, R. Liang, J. Li, R. Zheng, M. Li and J. Long, *J. Mater. Chem. A*, 2019, **7**, 21605.
27 X.-X. Wang, G.-J. Ji, P. She, F. Li, Q.-C. Liu, H.-F. Wang and J.-J. Xu, *Chem. Eng. J.*, 2021, **426**, 131101.
28 X. Chen, J. Chen, Y. Liu, Y. Liu, Y. Gao, S. Fan, X. He, X. Liu, C. Shen, Y. Jiang, L. Li, Y. Qiao and S. Chou, *ACS Appl. Mater. Interfaces*, 2023, **15**, 28106.
29 D. Lei, S. Ma, Y. Lu, Q. Liu and Z. Li, *J. Electron. Mater.*, 2019, **48**, 4653–4659.
30 Q. Liu, Z. Hu, L. Li, W. Li, C. Zou, H. Jin, S. Wang and S.-L. Chou, *ACS Appl. Mater. Interfaces*, 2021, **13**, 16585.
31 B. Ge, Y. Sun, J. Guo, X. Yan, C. Fernandez and Q. Peng, *Small*, 2019, **15**, e1902220.
32 Y. Mao, C. Tang, Z. Tang, J. Xie, Z. Chen, J. Tu, G. Cao and X. Zhao, *Energy Storage Mater.*, 2019, **18**, 405.
33 Z. Tang, M. Yuan, H. Zhu, G. Zeng, J. Liu, J. Duan and Z. Chen, *Front. Chem.*, 2021, **9**, 670612.
34 Q. Deng, Y. Yang, S. Qu, W. Wang, Y. Zhang and X. Ma, *Energy Storage Mater.*, 2021, **42**, 484.
35 J. Xia, Y. Zhou, J. Zhang, T. Lu, W. Gong, D. Zhang, X. Wang and J. Di, *Small*, 2023, **19**, 2301906.
36 X. Guo, T. Zheng, G. Ji, N. Hu, C. Xu and Y. Zhang, *J. Mater. Chem. A*, 2018, **6**, 10243.
37 M. Al-Dossary, A. A. Ismail, J. L. G. Fierro, H. Bouzid and S. A. Al-Sayari, *Appl. Catal., B*, 2015, **165**, 651.
38 J. Chen, X. Qi, C. Liu, J. Zeng and T. Liang, *ACS Appl. Mater. Interfaces*, 2020, **12**, 51418.
39 W. Ma, S. Lu, X. Lei, X. Liu and Y. Ding, *J. Mater. Chem. A*, 2018, **6**, 20829.
40 X. Zhang, C. Wang, H. Li, X.-G. Wang, Y.-N. Chen, Z. Xie and Z. Zhou, *J. Mater. Chem. A*, 2018, **6**, 2792.
41 L. Liu, L. Zhang, K. Wang, H. Wu, H. Mao, L. Li, Z. Sun, S. Lu, D. Zhang, W. Yu and S. Ding, *ACS Appl. Mater. Interfaces*, 2020, **12**, 33846.
42 S. Thoka, C.-J. Chen, A. Jena, F.-M. Wang, X.-C. Wang, H. Chang, S.-F. Hu and R.-S. Liu, *ACS Appl. Mater. Interfaces*, 2020, **12**, 17353.
43 Y. Qiao, J. Wu, J. Zhao, Q. Li, P. Zhang, C. Hao, X. Liu, S. Yang and Y. Liu, *Energy Storage Mater.*, 2020, **27**, 133.
44 D. Na, H. Jeong, J. Baek, H. Yu, S.-M. Lee, C.-R. Lee, H.-K. Seo, J.-K. Kim and I. Seo, *Electrochim. Acta*, 2022, **419**, 140408.
45 A. Bharti, G. Manna, P. Saha, G. Achutarao and A. J. Bhattacharyya, *J. Phys. Chem. Lett.*, 2022, **13**, 7380.
46 W. Ma, S. Lu, X. Lei, X. Liu and Y. Ding, *J. Mater. Chem. A*, 2018, **6**, 20829.
47 H. Liao, X. Guo, Y. Hou, H. Liang, Z. Zhou and H. Yang, *Small*, 2020, **16**, e1905223.